Improving the Stability of Diffusion Models for Content Consistent Super-Resolution

Lingchen Sun[1,2], Rongyuan Wu[1,2], Zhengqiang Zhang[1,2], Hongwei Yong[1], Lei Zhang[1,2*]
[1]The Hong Kong Polytechnic University [2]OPPO Research Institute

Abstract

The generative priors of pre-trained latent diffusion models have demonstrated great potential to enhance the perceptual quality of image super-resolution (SR) results. Unfortunately, the existing diffusion prior-based SR methods encounter a common problem, i.e., they tend to generate rather different outputs for the same low-resolution image with different noise samples. Such stochasticity is desired for text-to-image generation tasks but problematic for SR tasks, where the image contents are expected to be well preserved. To improve the stability of diffusion prior-based SR, we propose to employ the diffusion models to refine image structures, while employing the generative adversarial training to enhance image fine details. Specifically, we propose a non-uniform timestep learning strategy to train a compact diffusion network, which has high efficiency and stability to reproduce the image main structures, and fine-tune the pre-trained decoder of variational auto-encoder (VAE) by adversarial training for detail enhancement. Extensive experiments show that our proposed method, namely content consistent super-resolution (CCSR), can significantly reduce the stochasticity of diffusion prior-based SR, improving the content consistency of SR outputs and speeding up the image generation process. Codes and models can be found at https://github.com/csslc/CCSR.

1. Introduction

Images will be inevitably degraded during the acquisition process, and image super-resolution (SR) aims to recover a better quality high-resolution (HR) image from its low-resolution (LR) observation, which is a typical ill-posed problem [62]. Many of the previous deep learning-based SR methods [4, 9, 14, 17, 26, 28, 46, 56] assume simple and known image degradation (*e.g.*, bicubic down-sampling, down-sampling after Gaussian blur), while focus on the network backbone design, including those convolutional neural network (CNN) [4, 9, 17, 26, 46] and Transformer [6, 31, 75] based methods. However, there are always complex and unknown degradations in real-world applications, where the SR models trained with simple degradations often fail. It has become increasingly important to study real-world SR tasks. Some real-world LR-HR image paired datasets [3, 64] have been constructed, and some methods [58, 72] have been proposed to simulate more complex image degradations to approximate real-world scenarios.

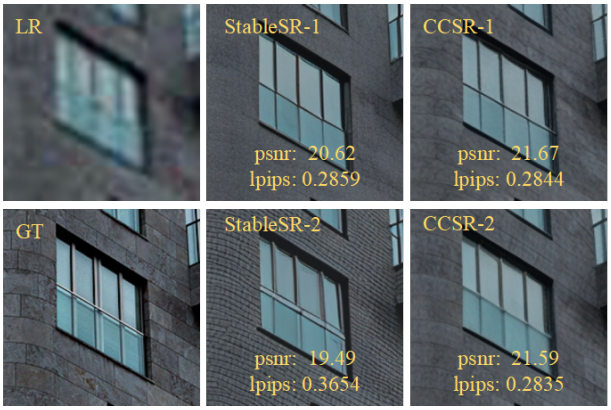

Figure 1. Visual comparisons of two super-resolution images with different starting points in the diffusion process from an input LR image. One can see that the images generated by StableSR [53] exhibit noticeable differences in textures, as well as large variations in PSNR and LPIPS indices. In contrast, our CCSR method produces more stable and content-consistent results.

It is well-known that the pixel-wise losses, *e.g.*, ℓ_1 loss and MSE loss, are prone to generating over-smoothed details in the SR outputs [33, 66]. The SSIM loss [60, 61] and perceptual loss [22] can alleviate this problem but the difficulties remain. On the other hand, the adversarial loss from the generative adversarial network (GAN) provides a much more effective solution, which has been widely used to reproduce richer and more realistic SR details [28, 32, 33, 56, 58]. While GAN and adversarial loss are very successful in reconstructing some specific classes of images such as face [18, 57, 67], they often result in unpleasant visual artifacts [13, 29, 33, 78] for natural images because the space of natural image priors is much bigger than that of specific classes.

*Corresponding author. This work is supported by the Hong Kong RGC RIF grant (R5001-18) and the PolyU-OPPO Joint Innovation Lab.

Recently, the Denoising Diffusion Probabilistic Model (DDPM) [20] and its variants [37, 48] have achieved unprecedented successes, offering a more competitive solution than GANs in numerous fields [7, 16, 45, 52, 63]. Compared to GANs, the diffusion model (DM) can learn priors with better diversity and quality, which have attracted significant attention from researchers in the image restoration field [30]. SR3 [45] applies DDPM for SR tasks by enabling conditional image generation through a stochastic iterative denoising process. Zero-shot image restoration methods, such as DDRM [24] and DDNM [59], integrate the powerful DM as a prior and incorporate the condition of low-quality images in the sampling process. However, these approaches can only deal with pre-defined linear or non-linear image degradations, and they cannot generalize to real-world SR tasks.

To handle the real-world complex degradations, some recent works [35, 53, 68], exploit the priors in the pre-trained text-to-image DM to generate the HR image by using the LR image as a condition. Though highly interesting results have been obtained, all those diffusion prior-based models share a limitation in generation stability and content consistency; that is, they tend to output different SR results for the same LR input with different noise samples. Fig. 1 shows an example by using StableSR [53] to restore an LR image. One can see that the two SR outputs of the same input exhibit very different textures, although they look realistic. Such kind of stochasticity of DM can be helpful for the text-to-image tasks [40, 73] to generate diverse outputs under a specific instruction, but it poses challenges for the SR tasks, where the image contents should not vary too much when enhancing image details.

In this paper, we propose a Content Consistent Super-Resolution (CCSR) approach to improve the stability of trained DM. Compared with GAN priors, diffusion priors are more powerful and flexible to facilitate the generation of more realistic and visually pleasing image content. This capability is especially useful when the LR image suffers from significant information loss and heavy degradation, for which the GAN-based models may fail. However, if the image structural contents can be well-reproduced, for example, by using the DM, the GAN network can subsequently enhance the details with low stochasticity. (Please refer to Sec. 3.1 and Fig. 2 for more discussions.) Motivated by this observation, we propose to leverage diffusion priors to generate coherent structures from the LR image, while employing generative adversarial training for detail and texture enhancement. To this end, we propose a non-uniform timestep sampling strategy in the diffusion stage, which simultaneously enhances the efficiency of information extraction and improves the stability of image structure generation. In the adversarial training stage, we finetune the pre-trained VAE decoder [42] to make it possess the capabilities of both latent feature decoding and detail enhancement without introducing additional computation burden. Equipped with the above strategies, our CCSR method can produce more stable and content-consistent SR results. In addition, it achieves appealing results with only 15 sampling steps, which is much faster than the existing diffusion prior-based SR methods.

2. Related Work

Image Super-Resolution. According to the research focuses, SR methods can be categorized into two major categories. The first category focuses on the network design by assuming simple and known image degradations to generate the LR-HR paired training data. The representative works in the first category include SRCNN [4] and DnCNN [71], which are among the earliest methods to employ CNNs for SR. After that, various novel strategies, such as dense [50], residual [34, 76, 77] and recursive connections [26] and non-local networks [39, 54], have been proposed to improve the CNN-based SR performance. With the attention mechanism to achieve global interaction, the transformer models [10, 36] have also been successfully employed for SR [6, 31, 75], resulting in much better performance than the CNN-based ones. The above methods basically aim for better image fidelity measures such as PSNR and SSIM [61] indices. To obtain visually more pleasing SR results with realistic details, GAN-based SR methods [2, 13, 21, 28, 29, 33, 56, 78], have been developed, which involve various improvements ranging from training strategies [2, 28, 56], architectural design [2, 28, 56] to loss functions [13, 21, 29, 33].

The second category focuses on how to improve the quality of real-world LR images, which have complex and even unknown degradations. Some researchers propose to collect real-world LR-HR paired datasets to train the network, such as RealSR [3], DRealSR [64], *etc*. However, this is very costly. A more economical way is to simulate real-world degradations using elegantly designed procedures. For example, BSRGAN [72] simulates real-world degradations by using a random shuffling strategy of basic degradation operators. RealESRGAN [58] uses a high-order degradation modeling by repeatedly applying a series of degradation operations. Both of them apply GAN for details generation. DASR [32] classifies the degradation space into three different levels and proposes a degradation-adaptive network. FeMaSR [5] regards SR as a feature-matching problem and introduces a pre-trained VQ-GAN [11, 69]. In general, the real-world SR methods sacrifice the fidelity measures to achieve better perceptual quality.

Diffusion SR Models. The GAN-based methods often introduce many visually unnatural artifacts while generating details. The recently developed generative DMs [20, 44, 48] provide a rescue. By encompassing a forward procedure

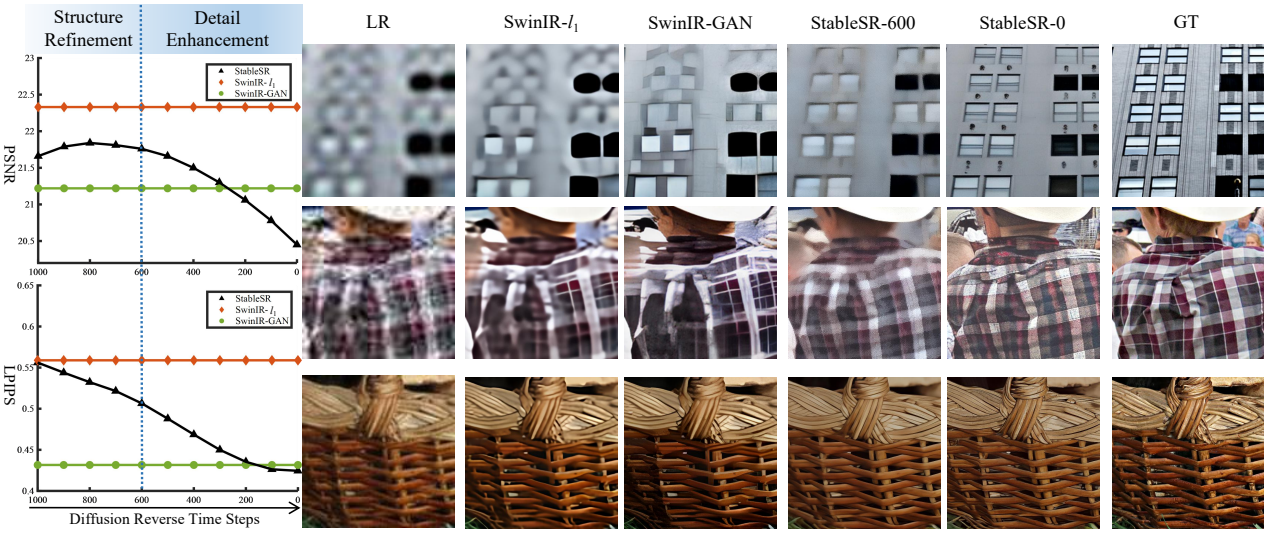

Figure 2. **Left**: PSNR and LPIPS indices of SR outputs by SwinIR-ℓ_1, SwinIR-GAN [31] and StableSR [53] at different steps on the DIV2K dataset. The PSNR index of StableSR increases in the early timesteps, implying structural refinement, but decreases in later timesteps, implying large structural changes. The LPIPS index of StableSR improves with timesteps, approaching that of SwinIR-GAN. **Right**: Visual comparisons of the SR results on three LR images. StableSR-600 and StableSR-0 mean the outputs at the 600-th timestep and the final output, respectively. When LR is corrupted heavily (first two rows), SwinIR-GAN struggles to generate fine details, while StableSR can produce more realistic results. However, when sufficient structural information is available in the LR image (bottom row), SwinIR-GAN performs similarly well to StableSR with faithful content.

that maps one data distribution to a target distribution, and a backward process that iteratively reverses the forward mapping, DDPM [20] has been successfully applied in various image generation applications [16, 40, 73]. To accelerate the sampling procedure in DDPM, the denoising diffusion implicit model (DDIM) [48] is proposed to replace the Markov forward process with a non-Markovian one. Furthermore, the latent diffusion model (LDM) [44] performs diffusion in the latent feature space defined by a VAE [42], which obtains faster training.

There are three main types of DM-based SR methods. The first type [12, 24, 59] modifies the reverse transition of a pre-trained DM using gradient descent. These methods are training-free but assume a pre-defined image degradation model. The second type [43, 47, 70, 79] retrains a DM from scratch on the paired training data. The third type [35, 53, 68] is to leverage the strong image priors of large-scale pre-trained DM, such as the text-to-image models [44], and introduce an adapter [40, 73] to fine-tune them. With the LR image as the control signal, high-quality SR outputs can be obtained. However, these methods suffer from the inconsistency and instability of SR results, which are the research focuses of this paper.

3. Methodology

3.1. Motivation and Framework

To improve the stability of diffusion priors to better assist SR tasks, we investigate in-depth how diffusion priors can help SR at different diffusion timesteps. In the left part of Fig. 2, we plot the PSNR and LPIPS indices of SR outputs by SwinIR-ℓ_1, SwinIR-GAN [31] and StableSR [53] at different timesteps on the DIV2K dataset. We see that the PSNR index of StableSR increases in the early steps, which implies structural refinement, but decreases in later steps, which implies large structural changes. The LPIPS index of StableSR continuously improves with time, approaching to that of SwinIR-GAN. It is not a surprise that SwinIR-ℓ_1 has a better PSNR index than the other two but its visual quality is the worst. In the right part of Fig. 2, we visualize the SR results of three LR images. When LR is corrupted heavily (first two rows), SwinIR-ℓ_1 fails to reproduce image structures and SwinIR-GAN struggles to generate fine details, while StableSR can produce more realistic results by exploiting the strong diffusion priors. However, when sufficient structural information is available in the LR image (bottom row), SwinIR-GAN performs similarly well to StableSR, and both of them can reconstruct the HR image with faithful contents.

The above observations motivate us to propose a new framework for a more stable and effective use of generative priors in SR. Our proposed framework, namely content-consistent super-resolution (CCSR), is shown in Fig. 3, which is built upon ControlNet [73] and pre-trained SD [44]. There are two training stages in CCSR, structure refinement (top left) and detail enhancement (top right). In the first stage, a non-uniform sampling strategy (bottom) is proposed, which applies one timestep to extract informa-

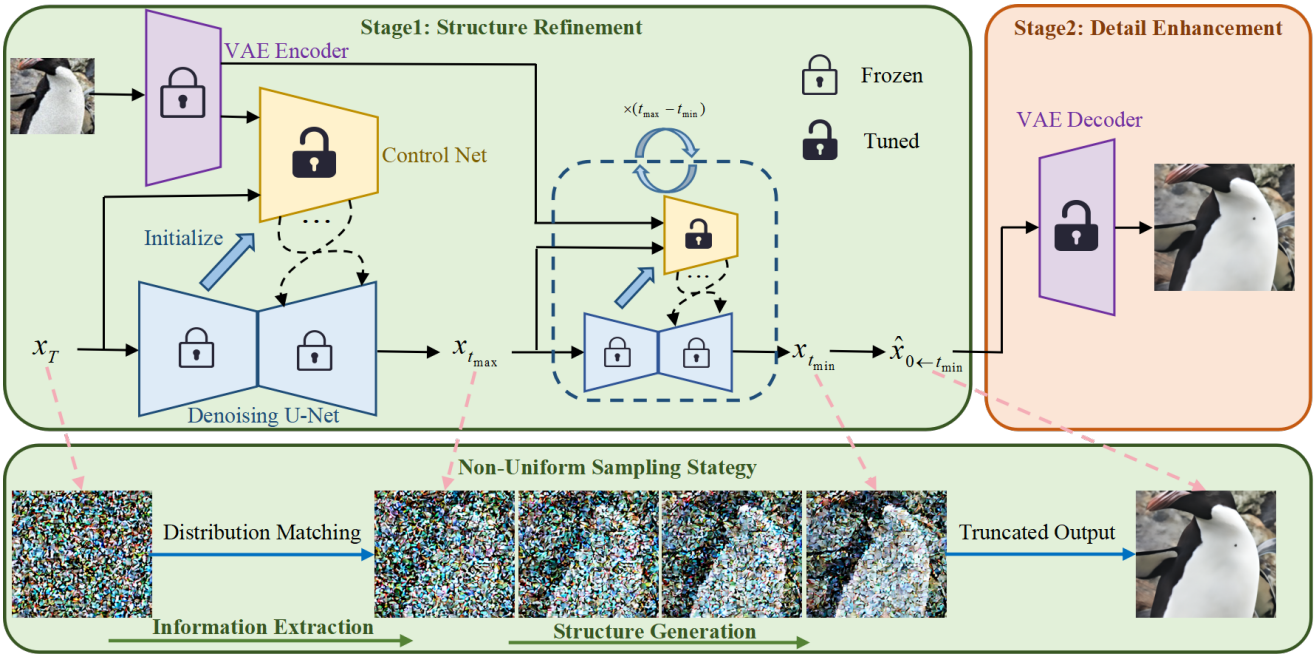

Figure 3. Framework of our proposed CCSR. There are two training stages in CCSR, structure refinement (top left) and detail enhancement (top right). In the first stage, a non-uniform sampling strategy (bottom) is proposed, which applies one timestep for information extraction from LR and several other timesteps for image structure generation. The diffusion process is then stopped and the truncated output is fed into the second stage, where the detail is enhanced by finetuning the VAE decoder with adversarial training.

tion from the LR input and several other timesteps for image structure generation. The diffusion process is then stopped and the truncated output is fed into the second stage, which aims to synthesize realistic details based on the structures reproduced in the first stage. Rather than employing an additional GAN network, we finetune the already existing VAE decoder with the adversarial loss so that it can perform feature decoding and detail enhancement simultaneously without introducing additional computational overhead. The two stages are detailed in the following sections.

3.2. Structure Refinement Stage

Preliminaries. DM employs a forward process to gradually transform an input image x_0 into Gaussian noise $x_T \sim N(0,1)$ in T steps: $x_t = \sqrt{1-\beta_t}\cdot x_{t-1} + \sqrt{\beta_t}\cdot\epsilon$, where x_t is the noisy image at step t, β_t controls the noise level, and ϵ is random noise following a standard normal distribution. This process can be reformulated as:

$$x_t = \sqrt{\bar{\alpha}_t}\cdot x_0 + \sqrt{1-\bar{\alpha}_t}\cdot\epsilon, \tag{1}$$

where $\alpha_t = 1-\beta_t$, and $\bar{\alpha}_t = \prod_{i=1}^{t}\alpha_i$.

The reverse process of DM iteratively recovers the original image x_0 sampled from $p(x_{t-1}|x_t, x_0) = N\left(x_{t-1}; \mu_t(x_t, x_0), \sigma_t^2\mathbf{I}\right)$. The mean of x_{t-1} is $\mu_t(x_t, x_0) = \frac{\sqrt{\bar{\alpha}_{t-1}}\beta_t}{1-\bar{\alpha}_t}x_0 + \frac{\sqrt{\alpha_t}(1-\bar{\alpha}_{t-1})}{1-\bar{\alpha}_t}x_t$, and the variance is $\sigma_t^2 = \frac{1-\bar{\alpha}_{t-1}}{1-\bar{\alpha}_t}\beta_t$. DM typically applies a denoising network $\epsilon_\theta(x_t, t)$ to estimate the noise so that the original image details can be reconstructed.

During DM training, the noisy image x_t is generated by randomly selecting a timestep $t \in [0, T)$ and noise $\epsilon \sim N(0,1)$ according to Eq. (1). The loss function l_{diff} is:

$$l_{diff} = \left\|\epsilon - \epsilon_\theta\left(\sqrt{\bar{\alpha}_t}\cdot x_0 + \sqrt{1-\bar{\alpha}_t}\cdot\epsilon, t\right)\right\|_2^2. \tag{2}$$

Non-Uniform Timestep Sampling. Most previous DM-based SR methods [35, 43, 53, 68, 70] follow the text-to-image generation methods [73] to employ a uniform sampling strategy with many iteration steps. However, text-to-image generation needs to generate almost every pixel from scratch, whereas in SR tasks an LR image is given, which provides a coarse structure for the desired image. The current noise sampling approaches do not fully take advantage of the LR input but iteratively generate the coarse structure, resulting in redundant computation and unwanted randomness. As shown in Fig. 1, with the conventional uniform sampling strategy, the SR results of StableSR [53] with two random noise samples can be very different in textures.

As mentioned in Sec. 3.1, based on the observations in Fig. 2, we propose to partition the diffusion process into two stages, as shown in Fig. 3. In the first stage of structure refinement, we propose a non-uniform sampling strategy to optimize the sampling process for SR tasks. For information extraction, only one timestep sampling is required to extract the coarse information from the LR image by mapping the Gaussian noise x_T to the intermediate noisy image $x_{t_{max}}$. For structure generation, the diffusion chain is truncated after a few uniform timesteps from $x_{t_{max}}$ to $x_{t_{min}}$.

The truncated approach is used since the structure has already been well reconstructed in the intermediate process (please refer to the results of StableSR-600 in Fig. 2). The estimated result from $x_{t_{min}}$, denoted as $\hat{x}_{0\leftarrow t_{\min}}$, is output to the second stage of detail enhancement by generative adversarial training.

Given $x_{t_{max}}$ and $x_{t_{min}}$, during the two intervals (T, t_{max}) and $(t_{min}, 0]$, there is no need of sampling in training. The sampling is only needed when $t = T$ and t fall into the range of $[t_{max}, t_{min}]$. The reverse process from x_T to $x_{t_{max}}$ can be traced by substituting the corresponding parameter in Eq. (1). However, the diffusion step from T to t_{max} is much bigger than the original step so the Gaussian noise assumption will not hold [65, 80]. Therefore, directly applying this nonuniform sampling strategy will lead to significant performance loss. Note that the intermediate diffusion processes in Fig. 3 are visualized by decoding.

To solve the above issue, we propose to constrain the estimated $\hat{x}_{0\leftarrow T}$ at $t = T$ rather than the sampled noise. Given a sampled start point x_T by Eq. (1), the estimated noise $\hat{\epsilon}_T$ can be obtained from the denoising network by $\hat{\epsilon}_T = \epsilon_\theta(x_T, T)$. Then $\hat{x}_{0\leftarrow T}$ can be calculated by $\hat{x}_{0\leftarrow T} = \frac{1}{\sqrt{\bar{\alpha}_T}}\left(x_T - \sqrt{1-\bar{\alpha}_T}\cdot\hat{\epsilon}_T\right)$. Consequently, the loss function for $t = T$ is $l_T = \|x_0 - \hat{x}_{0\leftarrow T}\|_2^2$. Using the estimated $\hat{x}_{0\leftarrow T}$, $\hat{x}_{t_{max}}$ can be obtained by adding the corresponding noise as $\hat{x}_{t_{max}} = \sqrt{\bar{\alpha}_{t_{max}}}\cdot\hat{x}_{0\leftarrow T} + \sqrt{1-\bar{\alpha}_{t_{max}}}\cdot\epsilon$. To preserve the continuity of the diffusion chain, we enforce the same constraint on $\hat{x}_{t_{max}}$ as that on x_T, leading to $l_{t_{\max}} = \left\|x_0 - \frac{1}{\sqrt{\bar{\alpha}_{t_{\max}}}}\left(\hat{x}_{t_{\max}} - \sqrt{1-\bar{\alpha}_{t_{\max}}}\hat{\epsilon}_{t_{max}}\right)\right\|_2^2$. In $l_{t_{max}}$, $\hat{\epsilon}_{t_{max}} = \epsilon_\theta(\hat{x}_{t_{max}}, t_{max})$. Finally, the training loss of CCSR at $t = T$ is:

$$l_{diff}^T = l_{diff} + l_T + l_{t_{\max}}. \tag{3}$$

Note that we do not change the loss function for the other sampling timesteps.

3.3. Detail Enhancement Stage

Based on the refined image structures in the first stage, we leverage adversarial training to enhance the fine details without introducing further randomness. While it is common to employ an additional module for enhancement [63, 70], we adopt a more efficient approach by fine-tuning the already existing VAE decoder. This is motivated by previous findings [38, 63, 81] that the VAE decoder has redundancy and untapped potential. In specific, we reuse the VAE decoder for decoding latent features as well as enhancing details. The training loss remains the same as that of VAE [42]. Remarkably, this simple strategy achieves outstanding performance, as demonstrated in our ablation study in Sec. 4.5 as well as in Fig. 1.

Remarks. We train Stage 1 of CCSR first, and take its output $\hat{x}_{0\leftarrow t_{\min}}$ as the input of the second stage. When Stage 2 is trained, all the parameters of the first stage are frozen. Because only a few (15 in our experiments) timesteps are used in the inference period of Stage 1, $\hat{x}_{0\leftarrow t_{\min}}$ can be iteratively obtained from x_T, making the training and inference more consistent. For the setting of t_{max} and t_{min}, we simply set them to $\frac{2T}{3}$ and $\frac{T}{3}$ in all our experiments. The selection of t_{min} and t_{max} will be discussed in Sec. 4.5.

4. Experiments

4.1. Experimental Setting

Training and Inference. CCSR is built upon LAControNet [35, 73] with Stable Diffusion (SD) 2.1-base [44]. We first finetune the pre-trained SD for 25K iterations. In the adversarial training of the VAE decoder, we finetune it for 100 iterations. Following [53, 68], we use DIV2K [1], Flick2k [49], DIV8K [15], OST [55] and the first 5K images in FFHQ [23] as the training data. The degradation pipeline in RealESRGAN [58] is used to generate the paired training data for comparisons on real-world SR tasks, and the bicubic degradation is used to generate the paired training data for the comparisons on bicubic SR tasks. The Adam [27] optimizer is used in optimizing the models, and the learning rates of the two training stages are $1e^{-4}$ and $5e^{-6}$. The batch size in both the two training stages is set as 192. The sizes of training patches are 512×512 for real-world SR tasks and 256×256 for bicubic SR tasks.

During inference, we use DDPM [20] with our proposed non-uniform sampling strategy, and we found that $T = 45$ with 15 diffusion steps is enough for our CCSR method to produce appealing visual and numerical results compared with other DM-based SR methods.

Compared Methods. For the task of real-world SR, we compare our CCSR with representative and state-of-the-art GAN-based and DM-based SR methods. The GAN-based SR methods include BSRGAN [72], RealESRGAN [58], LDL [33] and DASR [32], while the DM-based SR methods include LDM-SR [43], StableSR [53], ResShift [70], DiffBIR [35] and PASD [68]. For the task of classical SR (*i.e.*, with simple bicubic degradation), we compare CCSR with DDRM [24], DDNM [59] and SR3 [45]. The results of the compared methods in this paper are obtained by using publicly released codes or models. Since the official code of SR3 is unavailable, we train it from scratch based on the publicly released code[1].

Test Datasets. To comprehensively evaluate the effectiveness of our CCSR method, we conduct experiments on the following real-world and synthetic datasets.

- The cropped RealSR [3] and DRealSR [64] datasets re-

[1]https://github.com/Janspiry/Image-Super-Resolution-via-Iterative-Refinement

leased in [53], where the images suffer from real-world unknown degradations.
- The degraded DIV2K [1] test set in [53] following the degradation pipeline of RealESRGAN [58]. Note that most of the real-world SR methods [35, 53, 70] follow this pipeline (with different degradation parameters) to generate the training data.
- Degraded DIV2K test set using the degradation pipeline in BSRGAN [72], which is different from the pipeline in generating our training data. 1,000 LR-HR pairs are generated. This test set is to validate the robustness of various DM-based methods.
- ImageNet1K and DIV2K test sets using the bicubic degradation setting, which is used for the comparisons on the bicubic SR task.

4.2. Evaluation Metrics

Existing Quality Measures. Following previous arts [33, 53], we use the following reference and non-reference metrics to compare the performance of different methods:
- PSNR and SSIM [61], computed on the Y channel in the YCbCr space, to measure the fidelity of SR results.
- LPIPS [74] and DISTS [8], computed in the RGB space, to evaluate the perceptual quality of SR results.
- NIQE, CLIPIQA [51] and MUSIQ [25], which are no-reference image quality metrics.
- FID [19], computed in the RGB space, to measure the statistical distance between the real images and SR results using a pre-trained Inception network.

It should be noted that for those DM-based methods, each value of the above metrics is calculated by *averaging the results over 10 runs with 10 different noise samples*.

New Stability Measures. As mentioned in Sec. 1, most of the existing diffusion prior-based SR methods suffer from the stability problem, *i.e.*, they may generate rather different results with different noise samples (see Fig. 1 for example). Therefore, it is necessary to design measures to evaluate the stability of DM-based SR models.

We make such an attempt in this paper and propose two stability metrics, namely global standard deviation (**G-STD**) and local standard deviation (**L-STD**), to measure the image-level and pixel-level variations of the SR results. We run N times ($N = 10$ in our experiments) the experiments for each SR model on each test image within each test benchmark. For each SR image, we can compute its quality metrics (except for FID) and then calculate the STD values over the N runs for each metric. By averaging the STD values over all test images in a benchmark, the G-STD value of one metric, denoted by p, can be obtained:

$$\text{G-STD}^p = \frac{1}{M}\sum_{j=1}^{M}\sqrt{\frac{\sum_{i=1}^{N}(p_i^j - \bar{p}^j)^2}{N}}, \tag{4}$$

where p_i^j denotes the value of p for the restored image in the i-th run for the j-th image in a dataset with M images, and $\bar{p}^j$ is the average value of p^j over N runs.

G-STD reflects the stability of an SR model at the image level. To measure the stability at the local pixel level, we define L-STD, which computes the STD of pixels in the same location of the N SR images:

$$\text{L-STD} = \frac{1}{MHW}\sum_{j=1}^{M}\sum_{h=1}^{H}\sum_{w=1}^{W}\sqrt{\frac{\sum_{i=1}^{N}\left(x_{i,(h,w)}^j - \bar{x}_{(h,w)}^j\right)}{N}}, \tag{5}$$

where x_i^j denotes the restored image in the i-th run for the j-th image in a dataset, H and W denote image height and weight, (h, w) denote pixel location, and $\bar{x}_{(h,w)}$ is the mean of the N pixels at (h, w).

4.3. Comparisons on Real-world Super-Resolution

Quantitative Comparisons. DM-based methods can be further divided into two types. The first type uses an adapter [73] to finetune a pre-trained text-to-image diffusion model, including StableSR [53], DiffBIR [35], PASD [68] and our CCSR. Another type trains a model from scratch, including LDM-SR [43] and ResShift [70]. Specifically, LDM-SR applies the commonly-used diffusion framework, while ResShift redefines a diffusion reverse process for the SR task, which shows rather different behaviors from other DM-based methods. The results are shown in Table 1. We can have the following observations.

First, there are notable distinctions between GAN-based and DM-based SR methods. Due to the stronger generation capability, most of the DM-based methods demonstrate better performance in no-reference indices, such as NIQE, CLIPIQA, and MUSIQ, while sacrificing fidelity performance. For example, PASD [68] outperforms BSRGAN by about 5.5 in MUSIQ, while its PSNR is 1dB lower on the RealSR dataset. It is worth mentioning that the NIQE, CLIPIQA, and MUSIQ scores of the GT images in RealSR are 6.17, 0.4579, and 57.44, respectively, which actually lag behind the output of most DM-based methods. This partially explains why DM-based methods can synthesize better perceptual quality images than GAN-based ones but with worse fidelity measures. ResShift [70] uses a redefined diffusion chain for SR and trains the DM from scratch, achieving better fidelity indices but lower perceptual and visual (see next sub-section) quality performance.

Second, the proposed CCSR achieves outstanding fidelity and perceptual measures among all the DM-based methods. In terms of fidelity metrics PSNR/SSIM, CCSR is only slightly worse than ResShift. In terms of perceptual metrics LPIPS/DISTS, CCSR achieves the best or second scores across all test sets. For the no-reference metrics, CCSR obtains the best or second-best NIQE scores on all test sets except for RealSR and achieves comparable

Table 1. Quantitative comparison among the state-of-the-art methods on both synthetic and real-world test datasets. S denotes the number of diffusion reverse steps in the method. Note that the G-STD is not available for FID, because FID measures the statistical distance between two groups of images. The best and the second-best results are highlighted in red and blue, respectively.

Datasets	Metrics	BSRGAN	RealESRGAN	LDL	DASR	ResShift -S15	LDM-SR -S200	StableSR -S200	DiffBIR –S50	PASD -S20	CCSR -S15
DIV2K StableSR	↑ PSNR/G-STD ↓	24.60	24.33	23.85	24.50	24.69/0.2720	23.36/0.6232	23.31/0.4874	23.67/0.6910	23.14/0.5489	24.46/0.2500
	↑ SSIM/G-STD ↓	0.6268	0.6372	0.6345	0.6303	0.6175/0.0118	0.5758/0.0288	0.5728/0.0250	0.5653/0.0396	0.5489/0.0248	0.6113/0.0108
	↓ LPIPS/G-STD ↓	0.3361	0.3124	0.3270	0.3551	0.3374/0.0196	0.3227/0.0317	0.3129/0.0303	0.3541/0.0466	0.3607/0.0311	0.3045/0.0157
	↓ DISTS/G-STD ↓	0.2268	0.2135	0.2223	0.2419	0.2215/0.0116	0.1961/0.0171	0.2138/0.0166	0.2129/0.0220	0.2219/0.0142	0.2065/0.0100
	L-STD ↓	-	-	-	-	0.0340	0.0441	0.0411	0.0443	0.0430	0.0288
	FID ↓	44.22	37.64	42.28	49.16	36.01	36.21	24.67	30.93	29.32	27.01
	↓ NIQE/G-STD ↓	4.75	4.68	4.85	5.03	6.82/0.5025	5.53/0.6846	4.76/0.5673	4.71/0.7515	4.40/0.5747	4.61/0.3959
	↑ CLIPIQA/G-STD ↓	0.5204	0.5219	0.5075	0.4996	0.6089/0.0537	0.6242/0.0727	0.6682/0.0592	0.6652/0.0817	0.6711/0.0442	0.5367/0.0531
	↑ MUSIQ/G-STD ↓	61.16	60.92	59.93	55.12	60.92/2.7917	62.38/4.0236	65.63/3.4023	65.66/4.3691	68.83/2.2256	62.78/2.6894
DIV2K-BSRGAN	↑ PSNR/G-STD ↓	24.65	23.83	23.52	24.35	24.09/0.2217	23.01/0.6016	23.05/0.4228	22.95/0.6003	22.21/0.3558	23.94/0.2143
	↑ SSIM/G-STD ↓	0.6156	0.6152	0.6161	0.6189	0.5946/0.0112	0.5563/0.0350	0.5514/0.0284	0.5365/0.0393	0.5031/0.0215	0.5801/0.0128
	↓ LPIPS/G-STD ↓	0.3741	0.3968	0.4053	0.4538	0.4251/0.0220	0.4229/0.0457	0.4170/0.0369	0.4125/0.0462	0.4647/0.0277	0.3848/0.0189
	↓ DISTS/G-STD ↓	0.2585	0.2673	0.2739	0.3078	0.2661/0.0131	0.2594/0.0242	0.2727/0.0193	0.2396/0.0226	0.2776/0.0142	0.2580/0.0116
	L-STD ↓	-	-	-	-	0.0295	0.0374	0.0324	0.0374	0.0394	0.0246
	FID ↓	84.69	81.26	85.65	93.64	86.11	70.29	66.59	68.89	68.82	69.86
	↓ NIQE/G-STD ↓	4.98	5.58	5.69	6.15	7.38/0.5323	6.64/1.0161	5.74/0.8336	4.87/0.8054	5.23/0.6131	4.74/0.4517
	↑ CLIPIQA/G-STD ↓	0.5158	0.5164	0.5069	0.4179	0.5701/0.0566	0.5631/0.0842	0.5981/0.0700	0.6599/0.0795	0.6500/0.0424	0.5180/0.0518
	↑ MUSIQ/G-STD ↓	58.23	56.23	54.55	44.08	55.46/3.4615	53.67/6.4723	56.23/4.9351	64.09/4.6820	64.62/2.4261	57.14/3.4570
RealSR	↑ PSNR/G-STD ↓	26.39	25.69	25.28	27.02	26.31/0.2859	25.49/0.7152	24.69/0.5600	24.88/0.7956	25.22/0.5301	26.24/0.3660
	↑ SSIM/G-STD ↓	0.7654	0.7616	0.7567	0.7708	0.7411/0.0133	0.7159/0.0306	0.7052/0.0219	0.6673/0.0462	0.6809/0.0275	0.7365/0.0119
	↓ LPIPS/G-STD ↓	0.2670	0.2727	0.2766	0.3151	0.3489/0.0236	0.3129/0.0452	0.3091/0.0299	0.3567/0.0562	0.3392/0.0311	0.2559/0.0158
	↓ DISTS/G-STD ↓	0.2121	0.2063	0.2121	0.2207	0.2498/0.0093	0.2218/0.0180	0.2167/0.0152	0.2290/0.0225	0.2259/0.0130	0.1985/0.0112
	L-STD ↓	-	-	-	-	0.0240	0.0241	0.0300	0.0346	0.0304	0.0218
	FID ↓	141.28	135.18	142.71	132.63	142.81	132.32	127.20	124.56	123.08	105.55
	↓ NIQE/G-STD ↓	5.66	5.83	6.00	6.53	7.27/0.5592	6.41/0.9051	5.76/0.6691	5.63/1.0350	5.18/0.6650	5.74/0.6126
	↑ CLIPIQA/G-STD ↓	0.5001	0.4449	0.4477	0.3121	0.5450/0.0493	0.5906/0.0894	0.6195/0.0575	0.6412/0.0739	0.6502/0.0411	0.5287/0.0526
	↑ MUSIQ/G-STD ↓	63.21	60.18	60.82	40.79	58.10/2.5458	60.18/4.1886	65.42/3.1678	64.66/4.6444	68.74/2.1633	63.64/2.2287
DRealSR	↑ PSNR/G-STD ↓	28.75	28.64	28.21	29.77	28.45/0.4100	28.09/0.9090	28.04/0.7488	26.84/1.3261	27.48/0.6497	28.96/0.4441
	↑ SSIM/G-STD ↓	0.8031	0.8053	0.8126	0.8264	0.7632/0.0197	0.7487/0.0450	0.7460/0.0318	0.6660/0.0779	0.7051/0.0304	0.7710/0.0163
	↓ LPIPS/G-STD ↓	0.2883	0.2847	0.2815	0.3126	0.4073/0.0349	0.3352/0.0577	0.3354/0.0408	0.4446/0.0785	0.3854/0.0333	0.2922/0.0237
	↓ DISTS/G-STD ↓	0.2142	0.2089	0.2132	0.2271	0.2700/0.0132	0.2259/0.0229	0.2287/0.0190	0.2706/0.0328	0.2535/0.0147	0.2146/0.0105
	L-STD ↓	-	-	-	-	0.0241	0.0263	0.0257	0.0349	0.0289	0.0200
	FID ↓	155.63	147.62	155.53	155.28	175.92	157.31	147.03	167.38	157.36	132.73
	↓ NIQE/G-STD ↓	6.52	6.69	7.13	7.60	8.28/0.5985	7.03/0.9592	6.51/0.8212	6.02/1.1834	5.57/0.7560	5.91/0.7107
	↑ CLIPIQA/G-STD ↓	0.4915	0.4422	0.4310	0.3684	0.5259/0.0558	0.5668/0.0881	0.6171/0.0685	0.6292/0.0904	0.6714/0.0467	0.5467/0.0550
	↑ MUSIQ/G-STD ↓	57.14	54.18	53.85	42.23	49.86/3.5063	53.72/5.6887	58.50/4.6598	60.68/6.1450	64.55/2.7189	58.82/2.7434

MUSIQ scores across all test sets. CCSR performs less well on CLIPIQA, which is based on CLIP [41]. Note that CLIP is used to train SD [44]. Therefore, leveraging more diffusion prior is likely to have a better CLIPIQA score. CCSR leverages the diffusion prior only in the structure refinement stage and hence obtains a lower CLIPIQA index.

Last but not least, as a DM-based SR method, CCSR demonstrates much better stability in synthesizing image details, as evidenced by its outstanding G-STD and L-STD measures. Specifically, CCSR achieves the best L-STD scores on all the test sets, showcasing its strong capability in reducing the stochasticity of local structure and detail generation. It achieves most of the best G-STD scores on reference metrics, and the best or second-best G-STD scores on no-reference metrics, demonstrating high content consistency of SR outputs. Though ResShift also has good stability measures, its visual quality is less satisfactory (see Fig. 4). Note that PASD achieves the best G-STD scores on many no-reference metrics. This can be attributed to its use of high-level information, which helps generate high-quality images with similar no-reference scores, but the image contents can be very different (see Fig. 4).

Qualitative Comparisons. We present visual comparisons on both synthetic (first two groups) and real-world (last group) images in Fig. 4. Considering the stochasticity in DMs, the restored images with the best and worst PSNR values over 10 runs are presented for each DM-based SR method. One can see that GAN-based methods are difficult to generate textures from the degraded structures in the LR image, resulting in over-smoothed or even wrong details (*e.g.*, the windows in the first two groups and the line in the last group). Among the DM-based methods, LDM-SR and ResShift have relatively lower perceptual quality, failing to synthesize realistic structures (*e.g.*, window in the first image) or introducing visual artifacts (*e.g.*, color noise in the third image). StableSR, DiffBIR, and PASD can generate perceptually more realistic details by leveraging the strong diffusion priors in the pre-trained SD model; however, their outputs are not stable. The two results with the highest and lowest PSNR values can vary a lot. Fortunately, our proposed CCSR can not only produce high-quality realistic SR results but also have high stability. One can see that the two images with the best and worst PSNR values produced by CCSR among the 10 runs only vary a little in content.

More visual comparisons on synthetic and real-world images are presented in Fig. 5 and Fig. 6, respectively. As can be seen from these figures, our CCSR outperforms the other methods in terms of reconstructing more accurate

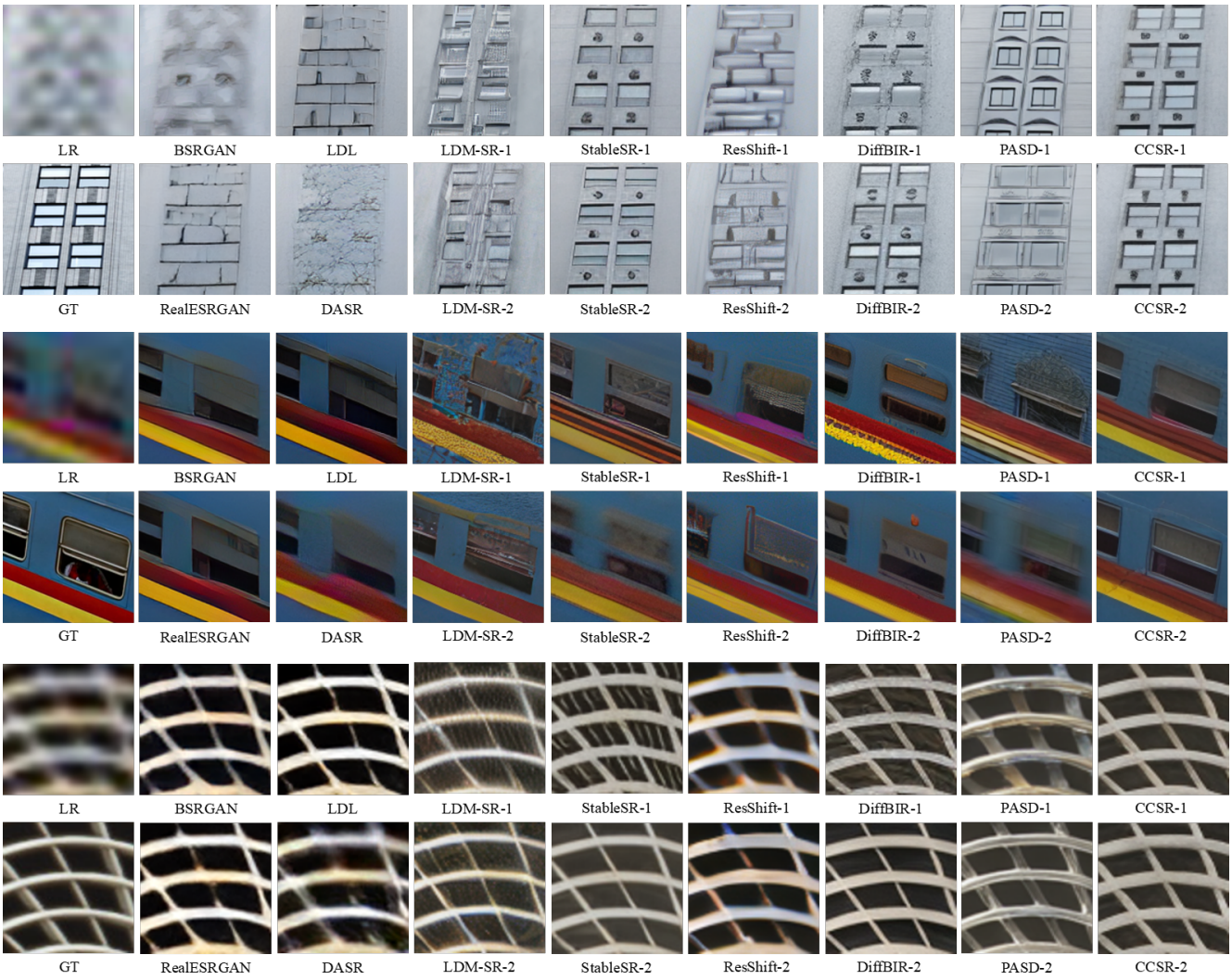

Figure 4. Visual comparisons (better zoom-in on screen) between our CCSR with state-of-the-art GAN-based and DM-based methods, including RealESRGAN [58], BSRGAN [72], DASR [32], LDL [33], LDM-SR [43], StableSR [53], ResShift [70], DiffBIR[35] and PASD [68]. For the DM-based method, two restored images that have the best and worst PSNR values over 10 runs are shown for a more comprehensive and fair comparison. Our proposed CCSR works the best in reconstructing more accurate structures and more realistic, content-consistent, and stable details.

Table 2. The inference time and the number of model parameters of DM-based methods. S denotes the number of diffusion reverse steps in the method.

	LDM-SR -S200	StableSR -S200	ResShift -S15	DiffBIR -S50	PASD -S20	CCSR -S15
Inference time(s)/Image	5.21	18.90	1.12	5.85	6.11	2.22
#Params(M)	168.95	1409.11	173.91	1716.71	1883.70	1700.91

structures, generating more realistic and content-consistent details, and reducing artifacts.

Inference Time. The number of parameters and the inference time of competing models are shown in Table 2. The inference time is calculated on the $\times 4$ SR task for 128×128 LR images with NVIDIA V100 32G GPU. StableSR, DiffBIR, PASD, and CCSR employ the pre-trained SD model and they have a similar amount of parameters. LDM-SR and ResShift are trained from scratch and have much fewer parameters. LDM-SR uses 200 diffusion steps, while ResShift uses 15 steps to achieve faster inference speed. Among the pre-trained SD-based methods, CCSR runs the fastest because it takes only 15 steps. Overall, CCSR has a comparable inference time with ResShift while achieving much better SR performance.

4.4. Comparisons on Bicubic Super-Resolution

We further conduct experiments to compare CCSR with those DM-based methods designed for classical SR tasks (*i.e.*, with simple bicubic degradation), including DDRM [24], DDNM [59] and SR3 [45].

The quantitative results are presented in Table 3. Since

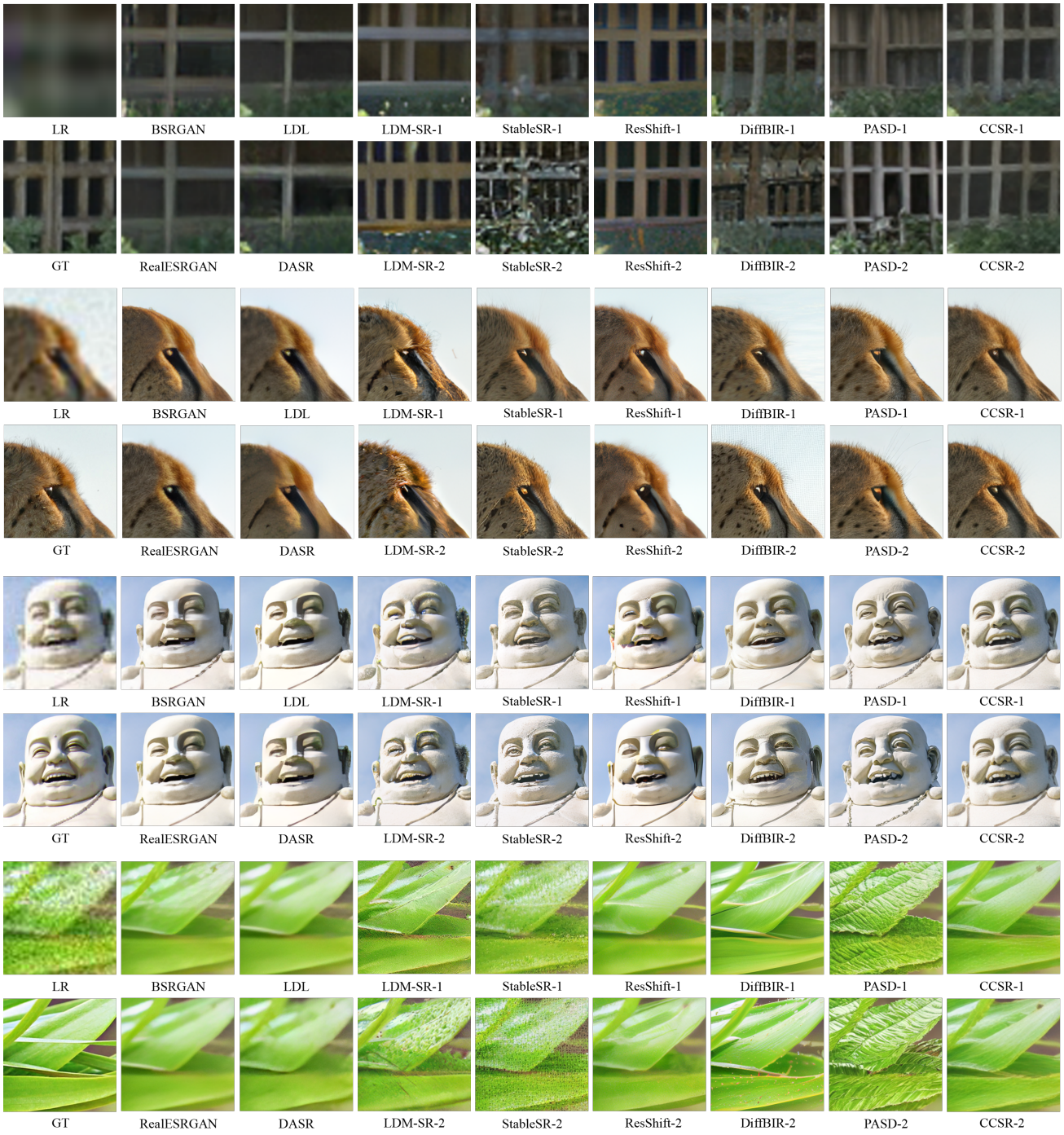

Figure 5. Visual comparisons (better zoom-in on screen) on synthetic data between CCSR and state-of-the-art GAN-based and DM-based methods, including RealESRGAN [58], BSRGAN [72], DASR [32], LDL [33], LDM-SR [43], StableSR [53], ResShift [70], DiffBIR[35] and PASD [68]. For the DM-based methods, two restored images that have the best and worst PSNR values over 10 runs are shown for a more comprehensive and fair comparison.

Figure 6. Visual comparisons (better zoom-in on screen) on real-world dataset between CCSR and state-of-the-art GAN-based and DM-based methods, including RealESRGAN [58], BSRGAN [72], DASR [32], LDL [33], LDM-SR [43], StableSR [53], ResShift [70], DiffBIR[35] and PASD [68]. For the DM-based methods, two restored images that have the best and worst PSNR values over 10 runs are shown for a more comprehensive and fair comparison.

Table 3. Quantitative comparisons between CCSR and DDRM [24], DDNM [59] and SR3 [45] on ImageNet and DIV2K datasets corrupted by bicubic degradation. The number of diffusion reverse steps for each method is also given. Note that the G-STD metric is not applicable for FID because FID measures the statistical distance between two groups of images. The best and the second-best results are highlighted in red and blue, respectively.

Datasets	Metrics	DDRM (20 steps)	DDNM (100 steps)	SR3 (200 steps)	CCSR (15 steps)
ImageNet 1K	↑ PSNR/G-STD ↓	28.15/0.1668	29.08/0.1527	26.02/0.2117	26.59/0.1258
	↑ SSIM/G-STD ↓	0.7816/0.0037	0.8032/0.0033	0.7197/0.0052	0.7229/0.0037
	↓ LPIPS/G-STD ↓	0.2205/0.0143	0.2491/0.0171	0.1718/0.0069	0.1558/0.0044
	↓ DISTS/G-STD ↓	0.1840/0.0072	0.1876/0.0056	0.1703/0.0059	0.1569/0.0044
	L-STD ↓	0.0113	0.0104	0.0229	0.0143
	FID ↓	42.65	41.70	50.99	43.43
	↓ NIQE/G-STD ↓	6.98/0.5627	10.15/1.6881	5.38/0.4306	5.89/0.3973
	↑ CLIPIQA/G-STD ↓	0.3395/0.0260	0.4822/0.0296	0.5370/0.0362	0.5598/0.0312
	↑ MUSIQ/G-STD ↓	31.71/2.2641	31.75/1.5592	51.16/2.1615	53.49/1.5777
DIV2K	↑ PSNR/G-STD ↓	29.73/0.1511	30.55/0.1478	27.94/0.2337	28.07/0.1365
	↑ SSIM/G-STD ↓	0.7742/0.0034	0.7935/0.0030	0.7276/0.0045	0.7205/0.0036
	↓LPIPS/G-STD ↓	0.2473/0.0132	0.2848/0.0182	0.1998/0.0067	0.1694/0.0051
	↓ DISTS/G-STD ↓	0.1910/0.0060	0.1959/0.0054	0.1799/0.0061	0.1620/0.0049
	L-STD ↓	0.0103	0.0092	0.0201	0.0136
	FID ↓	56.45	50.88	56.78	48.42
	↓ NIQE/G-STD ↓	8.33/0.6114	11.38/1.64	7.50/0.5459	7.60/0.5092
	↑ CLIPIQA/G-STD ↓	0.3239/0.0243	0.4844/0.0330	0.5261/0.0338	0.5377/ 0.0310
	↑ MUSIQ/G-STD ↓	30.59/1.7778	30.21/1.4911	44.71/1.8585	49.07/1.4386

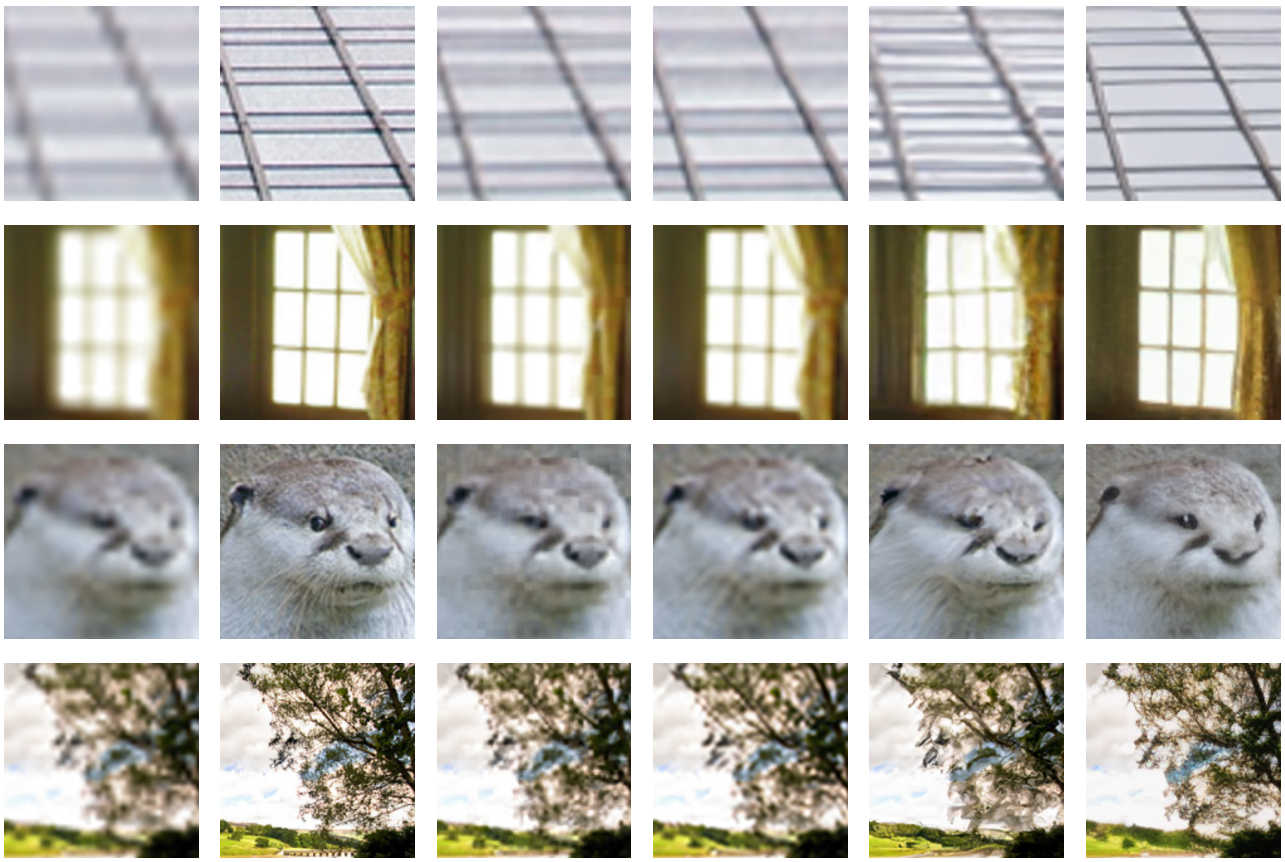

Figure 7. Visual comparisons (better zoom-in on screen) on the bicubic image SR task between CCSR and DDRM [24], DDNM [59] and SR3 [45]. For each method, the restored images with the best PSNR scores over 10 runs are shown for fair comparison.

Table 4. Ablation studies on the proposed non-uniform timestep learning (NUTL) and VAE decoder finetuning (DeFT) strategies on RealSR [3] and DIV2K-StableSR [1, 53] benchmarks. We implement two variants of CCSR. 'V1' means removing both NUTL and DeFT strategies, and 'V2' means removing the DeFT strategy only. The best results of each group are highlighted in bold.

Indices	Strategies		RealSR				DIV2K-StableSR			
	NUTL	DeFT	PSNR/G-STD	LPIPS/G-STD	MUSIQ/G-STD	L-STD	PSNR/G-STD	LPIPS/G-STD	MUSIQ/G-STD	L-STD
V1	×	×	25.87/0.4563	0.3257/0.0237	**66.08**/2.3880	0.0246	24.01/0.3375	0.3400/0.0265	**66.61/2.4915**	0.0307
V2	✓	×	**26.30**/0.3817	0.3057/0.0185	65.07/2.5185	0.0226	24.32/0.2708	0.3223/0.0190	65.47/2.5095	0.0294
CCSR	✓	✓	26.24/**0.3660**	**0.2559/0.0158**	63.63/**2.2287**	**0.0218**	**24.46/0.2500**	**0.3045/0.0157**	62.78/2.6894	**0.0288**

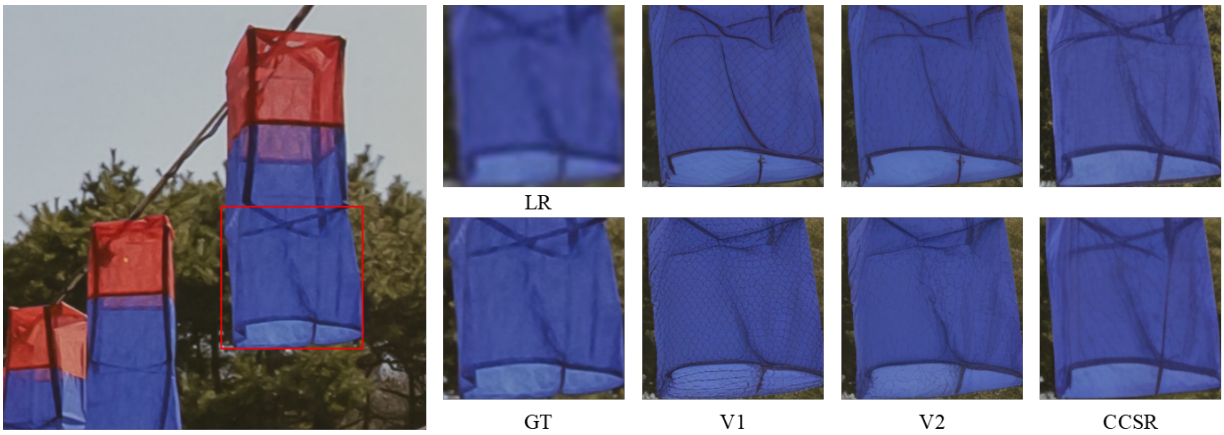

Figure 8. Visual comparisons of CCSR and its two variants 'V1' and 'V2' (better zoom-in on screen). For V1, V2 and the original CCSR, the two restored images with the best and worst PSNR scores over 10 runs are shown for a more comprehensive and fair comparison. One can see that the NUTL and DeFT strategies improve the super-resolution performance and stability.

DDRM, DDNM, and SR3 do not use the prior of pre-trained text-to-image models, they exhibit relatively stable performance in terms of G-STD and L-STD. Though our CCSR uses the diffusion prior of pre-trained text-to-image models, it still shows better stability than DDRM, DDNM, and SR3, demonstrating the effectiveness of our two-stage framework. SR3 and CCSR achieve lower fidelity metrics (PSNR/SSIM) than DDRM and DDNM because DDRM and DDNM leverage the known linear degradation operator in the zero-shot framework. CCSR and SR3 excel in terms of perceptual measures. In particular, CCSR demonstrates the best performance in most full-reference perceptual quality metrics (LPIPS/DISTS) and no-reference metrics (NIQE/CLIPIQA/MUSIQ).

Fig. 7 provides visual comparisons between CCSR and the other competing methods. For each method, the restored images with the best PSNR scores over 10 runs are shown for fair comparison. As can be seen, CCSR improves the structure preservation and clearness of the recovered images (the top two rows) and enhances the hair and texture details of animal and natural scene images (the bottom two rows).

4.5. Ablation Studies

The effectiveness of our proposed two strategies. In this part, we conduct ablation studies to evaluate the effectiveness of our proposed two strategies: the non-uniform timestep learning (NUTL) strategy in the structure refinement stage and the VAE decoder finetuning (DeFT) strategy in the detail enhancement stage. As shown in Table 4, we implement two variants of CCSR, *i.e.*, removing both NUTL and DeFT (see 'V1') and removing only DeFT (see 'V2'), while 'CCSR' represents the original CCSR method. We compare them on the RealSR [3] and DIV2K-StableSR [1, 53] datasets by using metrics of PSNR, LPIPS, MUSIQ, G-STD, and L-STD.

From Table 4, we can see that without the proposed NUTL and DeFT strategies, almost all the metrics become worse except for MUSIQ. This is because the no-reference metric MUSIQ prefers images with more high-frequency details, although those 'details' can be visually unpleasing artifacts. As can be seen in Fig. 8, the variant V1 generates many unfaithful patterns and textures. By introducing the NUTL strategy, the variant V2 can improve most of the metrics, and reduce the visual artifacts. Finally, by integrating both NUTL and DeFT into CCSR, most of the metrics are further improved (see Table 4), and the restored images showcase the best visual quality (see Fig. 8).

The selection of t_{max} and t_{min}. In our implementation of CCSR, we set the parameters t_{max} and t_{min} as $\frac{2T}{3}$

Table 5. Ablation studies on the selection of t_{max} and t_{min} on RealSR [3] and DIV2K-StableSR [1, 53] benchmarks. 'S' denotes the number of diffusion reverse steps in the method.

Indices	(t_{max},t_{min},S)	RealSR				DIV2K-StableSR			
		PSNR/G-STD	LPIPS/G-STD	MUSIQ/G-STD	L-STD	PSNR/G-STD	LPIPS/G-STD	MUSIQ/G-STD	L-STD
A1	(T/2, T/3, 8)	26.47/0.2534	0.2507/0.0107	62.95/1.8811	0.0184	24.82/ 0.2040	0.3059/0.0140	59.58/2.7610	0.0244
A2	(2T/3, T/2, 8)	26.22/0.3211	0.2496/0.0129	63.34/1.9586	0.0206	24.50/ 0.2426	0.3070/0.0149	61.67/2.4067	0.0268
A3	(4T/5, T/3, 21)	26.18/0.3819	0.2560/0.0162	63.72/2.3095	0.0219	24.49/0.2926	0.3016/0.0164	62.72/2.7343	0.0287
A4	(2T/3, T/5, 21)	26.38/0.3765	0.2616/0.0171	63.51/2.4664	0.0216	24.44/0.2896	0.3053/0.0190	63.58/2.7852	0.0299
CCSR	(2T/3, T/3, 15)	26.24/0.3660	0.2559/0.0158	63.64/2.2287	0.0218	24.46/0.2500	0.3045/0.0157	62.78/2.6894	0.0288

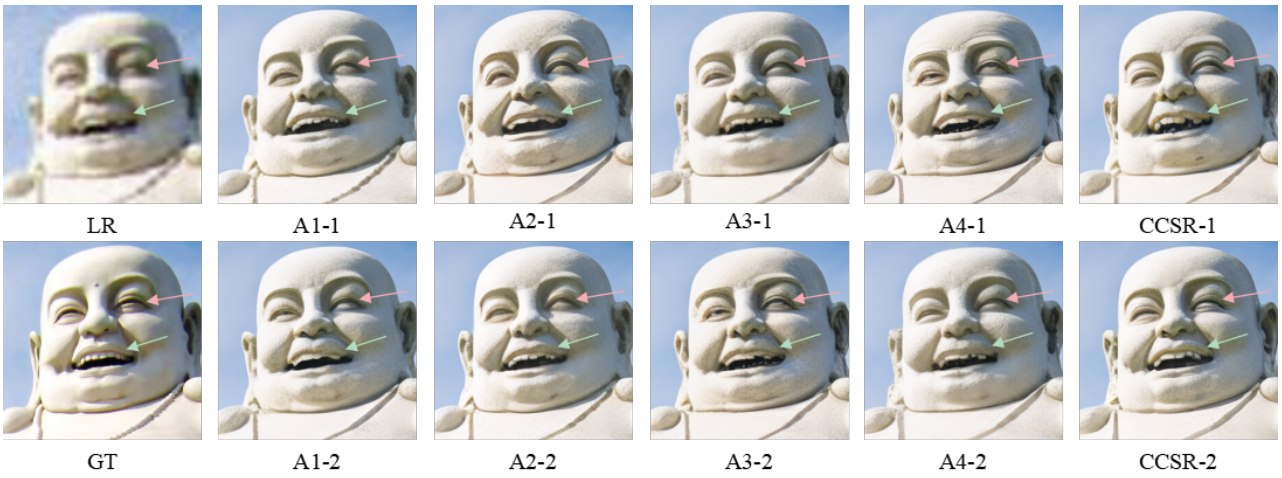

Figure 9. Visual comparisons of CCSR and its four variants 'A1', 'A2', 'A3' and 'A4' (better zoom-in on screen). For all compared methods, the two restored images with the best and worst PSNR scores over 10 runs are shown for a more comprehensive and fair comparison. One can see that different selections of t_{max}, t_{min} affect the SR performance to some extent.

and $\frac{T}{3}$, respectively. In Table 5, we test several alternative selections of them, *i.e.*, $t_{max}, t_{min} = \frac{T}{2}, \frac{T}{3}$ (see 'A1'), $t_{max}, t_{min} = \frac{2T}{3}, \frac{T}{2}$ (see 'A2'), $t_{max}, t_{min} = \frac{4T}{5}, \frac{T}{3}$ (see 'A3'), and $t_{max}, t_{min} = \frac{2T}{3}, \frac{T}{5}$ (see 'A4'). Since the number of diffusion reverse steps is directly determined by the difference between t_{max} and t_{min} (more steps for bigger difference), the numbers of diffusion reverse steps of 'A1', 'A2', 'A3', and 'A4' are 8, 8, 21 and 21, respectively. In addition, the visual comparisons between the four variants as well as CCSR are shown in Fig. 9.

We first compare 'A1', 'A3' and CCSR, which share the same t_{min} but vary in t_{max}. A larger t_{max} value results in more diffusion steps (*i.e.*, bigger 'S' value). One can see from Table 5 that a larger t_{max} leads to an improvement in no-reference metrics, which prefers more details. However, this increase in detail generation is accompanied by an increase in randomness, which adversely affects both stability performance and reference-based metrics. This phenomenon can be better observed in Fig. 9, where 'A1' obtains the best fidelity and stability performance. In specific, the teeth of the sculpture are all restored by 'A1', but there is a distortion in the eyes: the double eyelids are smoothed during the SR process. In contrast, the SR result of 'A3' has more details, but suffers from instability and fidelity. CCSR achieves a good balance between 'A1' and 'A3'. Similar observations can be made when comparing 'A2', 'A4', and CCSR, which have the same t_{max} but different t_{min} values. In summary, increasing the distance between t_{min} and t_{max} contributes to generating more details but leads to a decline in stability and fidelity.

We then compare 'A1' and 'A2', and compare 'A3' and 'A4', separately, which have the same 'S' value but different t_{max} and t_{min} values. A larger t_{max} value implies a higher intensity of added noise, facilitating the generation of more details. As a result, the no-reference metrics can be enhanced. Nevertheless, some unwanted details can also be introduced (see Fig. 9), leading to a degradation in perceptual quality and a simultaneous deterioration in both stability and reference-based metrics.

To sum up, different perception-distortion preferences can be obtained by choosing different combinations of t_{max} and t_{min}. From the numerical comparisons in Table 5 and visual comparisons in Fig. 9, $t_{max}, t_{min} = \frac{2T}{3}, \frac{T}{3}$

can achieve a relatively balanced result in perceptual quality, reference, and no-reference metrics, as well as computational complexity (*i.e.*, the diffusion reverse steps 'S'). Therefore, we adopt this setting in our experiments.

5. Conclusion

The strong generative priors of DMs can help synthesize realistic details for image SR tasks but the stochasticity of DMs induces the instability of SR outputs. To improve the stability of DM-based SR, we investigated in-depth how the diffusion priors can help the SR task at different diffusion steps. We found that diffusion priors are more powerful than GAN priors in generating image main structures when the LR image suffers from significant information loss. However, GAN performs similarly well to DM when the main structural information is available in the LR image. Based on this observation, we proposed the Content Consistent Super-Resolution (CCSR) approach. Firstly, the coherent structures were generated from the LR image by a diffusion stage. Then, the diffusion process was stopped and the truncated output was sent to the VAE decoder, which was finetuned via adversarial training to acquire the detail enhancement capability without extra computation burden. Extensive experiments demonstrated the superiority of the proposed CCSR method against the existing DM-based methods in numerical, visual, stability, and efficiency performance.

References

[1] Eirikur Agustsson and Radu Timofte. NTIRE 2017 challenge on single image super-resolution: Dataset and study. In *Proceedings of the IEEE conference on computer vision and pattern recognition workshops*, pages 126–135, 2017. 5, 6, 12, 13

[2] Yochai Blau and Tomer Michaeli. The perception-distortion tradeoff. In *Proceedings of the IEEE conference on computer vision and pattern recognition*, pages 6228–6237, 2018. 2

[3] Jianrui Cai, Hui Zeng, Hongwei Yong, Zisheng Cao, and Lei Zhang. Toward real-world single image super-resolution: A new benchmark and a new model. In *Proceedings of the IEEE/CVF International Conference on Computer Vision (ICCV)*, 2019. 1, 2, 5, 12, 13

[4] Dong Chao, Loy Chen Change, He Kaiming, and Tang Xiaoou. Learning a deep convolutional network for image super-resolution. In *ECCV*, pages 184–199, 2014. 1, 2

[5] Chaofeng Chen, Xinyu Shi, Yipeng Qin, Xiaoming Li, Xiaoguang Han, Tao Yang, and Shihui Guo. Real-world blind super-resolution via feature matching with implicit high-resolution priors. In *Proceedings of the 30th ACM International Conference on Multimedia*, pages 1329–1338, 2022. 2

[6] Xiangyu Chen, Xintao Wang, Jiantao Zhou, Yu Qiao, and Chao Dong. Activating more pixels in image super-resolution transformer. In *Proceedings of the IEEE/CVF Conference on Computer Vision and Pattern Recognition*, pages 22367–22377, 2023. 1, 2

[7] Prafulla Dhariwal and Alexander Nichol. Diffusion models beat gans on image synthesis. *Advances in neural information processing systems*, 34:8780–8794, 2021. 2

[8] Keyan Ding, Kede Ma, Shiqi Wang, and Eero P Simoncelli. Image quality assessment: Unifying structure and texture similarity. *IEEE transactions on pattern analysis and machine intelligence*, 44(5):2567–2581, 2020. 6

[9] Chao Dong, Chen Change Loy, and Xiaoou Tang. Accelerating the super-resolution convolutional neural network. In *European conference on computer vision*, pages 391–407. Springer, 2016. 1

[10] Alexey Dosovitskiy, Lucas Beyer, Alexander Kolesnikov, Dirk Weissenborn, Xiaohua Zhai, Thomas Unterthiner, Mostafa Dehghani, Matthias Minderer, Georg Heigold, Sylvain Gelly, et al. An image is worth 16x16 words: Transformers for image recognition at scale. *arXiv preprint arXiv:2010.11929*, 2020. 2

[11] Patrick Esser, Robin Rombach, and Bjorn Ommer. Taming transformers for high-resolution image synthesis. In *Proceedings of the IEEE/CVF conference on computer vision and pattern recognition*, pages 12873–12883, 2021. 2

[12] Ben Fei, Zhaoyang Lyu, Liang Pan, Junzhe Zhang, Weidong Yang, Tianyue Luo, Bo Zhang, and Bo Dai. Generative diffusion prior for unified image restoration and enhancement. In *Proceedings of the IEEE/CVF Conference on Computer Vision and Pattern Recognition*, pages 9935–9946, 2023. 3

[13] Dario Fuoli, Luc Van Gool, and Radu Timofte. Fourier space losses for efficient perceptual image super-resolution. In *Proceedings of the IEEE/CVF International Conference on Computer Vision*, pages 2360–2369, 2021. 1, 2

[14] Jinjin Gu, Hannan Lu, Wangmeng Zuo, and Chao Dong. Blind super-resolution with iterative kernel correction. In *Proceedings of the IEEE/CVF Conference on Computer Vision and Pattern Recognition*, pages 1604–1613, 2019. 1

[15] Shuhang Gu, Andreas Lugmayr, Martin Danelljan, Manuel Fritsche, Julien Lamour, and Radu Timofte. Div8k: Diverse 8k resolution image dataset. In *2019 IEEE/CVF International Conference on Computer Vision Workshop (ICCVW)*, pages 3512–3516. IEEE, 2019. 5

[16] Lanqing Guo, Chong Wang, Wenhan Yang, Siyu Huang, Yufei Wang, Hanspeter Pfister, and Bihan Wen. Shadowdiffusion: When degradation prior meets diffusion model for shadow removal. In *Proceedings of the IEEE/CVF Conference on Computer Vision and Pattern Recognition*, pages 14049–14058, 2023. 2, 3

[17] Muhammad Haris, Gregory Shakhnarovich, and Norimichi Ukita. Deep back-projection networks for super-resolution. In *Proceedings of the IEEE conference on computer vision and pattern recognition*, pages 1664–1673, 2018. 1

[18] Jingwen He, Wu Shi, Kai Chen, Lean Fu, and Chao Dong. Gcfsr: a generative and controllable face super resolution method without facial and gan priors. In *Proceedings of the IEEE/CVF Conference on Computer Vision and Pattern Recognition*, pages 1889–1898, 2022. 1

[19] Martin Heusel, Hubert Ramsauer, Thomas Unterthiner, Bernhard Nessler, and Sepp Hochreiter. Gans trained by a

two time-scale update rule converge to a local nash equilibrium. *Advances in neural information processing systems*, 30, 2017. 6

[20] Jonathan Ho, Ajay Jain, and Pieter Abbeel. Denoising diffusion probabilistic models. *Advances in neural information processing systems*, 33:6840–6851, 2020. 2, 3, 5

[21] Huaibo Huang, Ran He, Zhenan Sun, and Tieniu Tan. Wavelet-SRNET: A wavelet-based CNN for multi-scale face super resolution. In *Proceedings of the IEEE International Conference on Computer Vision*, pages 1689–1697, 2017. 2

[22] Justin Johnson, Alexandre Alahi, and Li Fei-Fei. Perceptual losses for real-time style transfer and super-resolution. In *European conference on computer vision*, pages 694–711. Springer, 2016. 1

[23] Tero Karras, Samuli Laine, and Timo Aila. A style-based generator architecture for generative adversarial networks. In *Proceedings of the IEEE/CVF conference on computer vision and pattern recognition*, pages 4401–4410, 2019. 5

[24] Bahjat Kawar, Michael Elad, Stefano Ermon, and Jiaming Song. Denoising diffusion restoration models. *Advances in Neural Information Processing Systems*, 35:23593–23606, 2022. 2, 3, 5, 8, 11

[25] Junjie Ke, Qifei Wang, Yilin Wang, Peyman Milanfar, and Feng Yang. Musiq: Multi-scale image quality transformer. In *Proceedings of the IEEE/CVF International Conference on Computer Vision*, pages 5148–5157, 2021. 6

[26] Jiwon Kim, Jung Kwon Lee, and Kyoung Mu Lee. Deeply-recursive convolutional network for image super-resolution. In *Proceedings of the IEEE conference on computer vision and pattern recognition*, pages 1637–1645, 2016. 1, 2

[27] Diederik P Kingma and Jimmy Ba. Adam: A method for stochastic optimization. *arXiv preprint arXiv:1412.6980*, 2014. 5

[28] Christian Ledig, Lucas Theis, Ferenc Huszár, Jose Caballero, Andrew Cunningham, Alejandro Acosta, Andrew Aitken, Alykhan Tejani, Johannes Totz, Zehan Wang, et al. Photo-realistic single image super-resolution using a generative adversarial network. In *Proceedings of the IEEE conference on computer vision and pattern recognition*, pages 4681–4690, 2017. 1, 2

[29] Wenbo Li, Kun Zhou, Lu Qi, Liying Lu, and Jiangbo Lu. Best-Buddy GANs for highly detailed image super-resolution. In *Proceedings of the AAAI Conference on Artificial Intelligence*, pages 1412–1420, 2022. 1, 2

[30] Xin Li, Yulin Ren, Xin Jin, Cuiling Lan, Xingrui Wang, Wenjun Zeng, Xinchao Wang, and Zhibo Chen. Diffusion models for image restoration and enhancement–a comprehensive survey. *arXiv preprint arXiv:2308.09388*, 2023. 2

[31] Jingyun Liang, Jiezhang Cao, Guolei Sun, Kai Zhang, Luc Van Gool, and Radu Timofte. SwinIR: Image restoration using swin transformer. In *Proceedings of the IEEE/CVF International Conference on Computer Vision*, pages 1833–1844, 2021. 1, 2, 3

[32] Jie Liang, Hui Zeng, and Lei Zhang. Efficient and degradation-adaptive network for real-world image super-resolution. In *European Conference on Computer Vision*, 2022. 1, 2, 5, 8, 9, 10

[33] Jie Liang, Hui Zeng, and Lei Zhang. Details or Artifacts: A locally discriminative learning approach to realistic image super-resolution. In *Proceedings of the IEEE/CVF Conference on Computer Vision and Pattern Recognition*, pages 5657–5666, 2022. 1, 2, 5, 6, 8, 9, 10

[34] Bee Lim, Sanghyun Son, Heewon Kim, Seungjun Nah, and Kyoung Mu Lee. Enhanced deep residual networks for single image super-resolution. In *Proceedings of the IEEE conference on computer vision and pattern recognition workshops*, pages 136–144, 2017. 2

[35] Xinqi Lin, Jingwen He, Ziyan Chen, Zhaoyang Lyu, Ben Fei, Bo Dai, Wanli Ouyang, Yu Qiao, and Chao Dong. Diffbir: Towards blind image restoration with generative diffusion prior. *arXiv preprint arXiv:2308.15070*, 2023. 2, 3, 4, 5, 6, 8, 9, 10

[36] Ze Liu, Yutong Lin, Yue Cao, Han Hu, Yixuan Wei, Zheng Zhang, Stephen Lin, and Baining Guo. Swin transformer: Hierarchical vision transformer using shifted windows. In *Proceedings of the IEEE/CVF international conference on computer vision*, pages 10012–10022, 2021. 2

[37] Cheng Lu, Yuhao Zhou, Fan Bao, Jianfei Chen, Chongxuan Li, and Jun Zhu. Dpm-solver: A fast ode solver for diffusion probabilistic model sampling in around 10 steps. *Advances in Neural Information Processing Systems*, 35:5775–5787, 2022. 2

[38] Feng Luo, Jinxi Xiang, Jun Zhang, Xiao Han, and Wei Yang. Image super-resolution via latent diffusion: A sampling-space mixture of experts and frequency-augmented decoder approach. 2023. 5

[39] Yiqun Mei, Yuchen Fan, and Yuqian Zhou. Image super-resolution with non-local sparse attention. In *Proceedings of the IEEE/CVF Conference on Computer Vision and Pattern Recognition*, pages 3517–3526, 2021. 2

[40] Chong Mou, Xintao Wang, Liangbin Xie, Jian Zhang, Zhongang Qi, Ying Shan, and Xiaohu Qie. T2i-adapter: Learning adapters to dig out more controllable ability for text-to-image diffusion models. *arXiv preprint arXiv:2302.08453*, 2023. 2, 3

[41] Alec Radford, Jong Wook Kim, Chris Hallacy, Aditya Ramesh, Gabriel Goh, Sandhini Agarwal, Girish Sastry, Amanda Askell, Pamela Mishkin, Jack Clark, et al. Learning transferable visual models from natural language supervision. In *International conference on machine learning*, pages 8748–8763. PMLR, 2021. 7

[42] Ali Razavi, Aaron Van den Oord, and Oriol Vinyals. Generating diverse high-fidelity images with vq-vae-2. *Advances in neural information processing systems*, 32, 2019. 2, 3, 5

[43] Robin Rombach, Andreas Blattmann, Dominik Lorenz, Patrick Esser, and Björn Ommer. High-resolution image synthesis with latent diffusion models. In *Proceedings of the IEEE/CVF conference on computer vision and pattern recognition*, pages 10684–10695, 2022. 3, 4, 5, 6, 8, 9, 10

[44] Robin Rombach, Andreas Blattmann, Dominik Lorenz, Patrick Esser, and Björn Ommer. High-resolution image synthesis with latent diffusion models. In *Proceedings of the IEEE/CVF conference on computer vision and pattern recognition*, pages 10684–10695, 2022. 2, 3, 5, 7

[45] Chitwan Saharia, Jonathan Ho, William Chan, Tim Salimans, David J Fleet, and Mohammad Norouzi. Image super-resolution via iterative refinement. *IEEE Transactions on Pattern Analysis and Machine Intelligence*, 45(4):4713–4726, 2022. 2, 5, 8, 11

[46] Mehdi SM Sajjadi, Bernhard Scholkopf, and Michael Hirsch. EnhanceNet: Single image super-resolution through automated texture synthesis. In *Proceedings of the IEEE international conference on computer vision*, pages 4491–4500, 2017. 1

[47] Shuyao Shang, Zhengyang Shan, Guangxing Liu, and Jinglin Zhang. Resdiff: Combining cnn and diffusion model for image super-resolution. *arXiv preprint arXiv:2303.08714*, 2023. 3

[48] Jiaming Song, Chenlin Meng, and Stefano Ermon. Denoising diffusion implicit models. *arXiv preprint arXiv:2010.02502*, 2020. 2, 3

[49] Radu Timofte, Eirikur Agustsson, Luc Van Gool, Ming-Hsuan Yang, and Lei Zhang. Ntire 2017 challenge on single image super-resolution: Methods and results. In *Proceedings of the IEEE conference on computer vision and pattern recognition workshops*, pages 114–125, 2017. 5

[50] Tong Tong, Gen Li, Xiejie Liu, and Qinquan Gao. Image super-resolution using dense skip connections. In *Proceedings of the IEEE international conference on computer vision*, pages 4799–4807, 2017. 2

[51] Jianyi Wang, Kelvin CK Chan, and Chen Change Loy. Exploring clip for assessing the look and feel of images. In *Proceedings of the AAAI Conference on Artificial Intelligence*, pages 2555–2563, 2023. 6

[52] Jinglong Wang, Xiawei Li, Jing Zhang, Qingyuan Xu, Qin Zhou, Qian Yu, Lu Sheng, and Dong Xu. Diffusion model is secretly a training-free open vocabulary semantic segmenter. *arXiv preprint arXiv:2309.02773*, 2023. 2

[53] Jianyi Wang, Zongsheng Yue, Shangchen Zhou, Kelvin CK Chan, and Chen Change Loy. Exploiting diffusion prior for real-world image super-resolution. *arXiv preprint arXiv:2305.07015*, 2023. 1, 2, 3, 4, 5, 6, 8, 9, 10, 12, 13

[54] Risheng Wang, Tao Lei, Wenzheng Zhou, Qi Wang, Hongying Meng, and Asoke K Nandi. Lightweight non-local network for image super-resolution. In *ICASSP 2021-2021 IEEE International Conference on Acoustics, Speech and Signal Processing (ICASSP)*, pages 1625–1629. IEEE, 2021. 2

[55] Xintao Wang, Ke Yu, Chao Dong, and Chen Change Loy. Recovering realistic texture in image super-resolution by deep spatial feature transform. In *Proceedings of the IEEE conference on computer vision and pattern recognition*, pages 606–615, 2018. 5

[56] Xintao Wang, Ke Yu, Shixiang Wu, Jinjin Gu, Yihao Liu, Chao Dong, Yu Qiao, and Chen Change Loy. ESRGAN: Enhanced super-resolution generative adversarial networks. In *Proceedings of the European conference on computer vision (ECCV) workshops*, pages 0–0, 2018. 1, 2

[57] Xintao Wang, Yu Li, Honglun Zhang, and Ying Shan. Towards real-world blind face restoration with generative facial prior. In *Proceedings of the IEEE/CVF conference on computer vision and pattern recognition*, pages 9168–9178, 2021. 1

[58] Xintao Wang, Liangbin Xie, Chao Dong, and Ying Shan. Real-esrgan: Training real-world blind super-resolution with pure synthetic data. In *Proceedings of the IEEE/CVF international conference on computer vision*, pages 1905–1914, 2021. 1, 2, 5, 6, 8, 9, 10

[59] Yinhuai Wang, Jiwen Yu, and Jian Zhang. Zero-shot image restoration using denoising diffusion null-space model. *arXiv preprint arXiv:2212.00490*, 2022. 2, 3, 5, 8, 11

[60] Zhou Wang, Eero P Simoncelli, and Alan C Bovik. Multiscale structural similarity for image quality assessment. In *The Thrity-Seventh Asilomar Conference on Signals, Systems & Computers, 2003*, pages 1398–1402. Ieee, 2003. 1

[61] Zhou Wang, Alan C Bovik, Hamid R Sheikh, and Eero P Simoncelli. Image quality assessment: from error visibility to structural similarity. *IEEE transactions on image processing*, 13(4):600–612, 2004. 1, 2, 6

[62] Zhihao Wang, Jian Chen, and Steven C. H. Hoi. Deep learning for image super-resolution: A survey. *IEEE Transactions on Pattern Analysis and Machine Intelligence*, 43(10):3365–3387, 2021. 1

[63] Zhixin Wang, Ziying Zhang, Xiaoyun Zhang, Huangjie Zheng, Mingyuan Zhou, Ya Zhang, and Yanfeng Wang. Dr2: Diffusion-based robust degradation remover for blind face restoration. In *Proceedings of the IEEE/CVF Conference on Computer Vision and Pattern Recognition*, pages 1704–1713, 2023. 2, 5

[64] Pengxu Wei, Ziwei Xie, Hannan Lu, Zongyuan Zhan, Qixiang Ye, Wangmeng Zuo, and Liang Lin. Component divide-and-conquer for real-world image super-resolution. In *Computer Vision–ECCV 2020: 16th European Conference, Glasgow, UK, August 23–28, 2020, Proceedings, Part VIII 16*, pages 101–117. Springer, 2020. 1, 2, 5

[65] Zhisheng Xiao, Karsten Kreis, and Arash Vahdat. Tackling the generative learning trilemma with denoising diffusion gans. *arXiv preprint arXiv:2112.07804*, 2021. 5

[66] Tianshuo Xu, Peng Mi, Xiawu Zheng, Lijiang Li, Fei Chao, Guannan Jiang, Wei Zhang, Yiyi Zhou, and Rongrong Ji. What hinders perceptual quality of PSNR-oriented methods? *arXiv preprint arXiv:2201.01034*, 2022. 1

[67] Tao Yang, Peiran Ren, Xuansong Xie, and Lei Zhang. Gan prior embedded network for blind face restoration in the wild. In *Proceedings of the IEEE/CVF Conference on Computer Vision and Pattern Recognition*, pages 672–681, 2021. 1

[68] Tao Yang, Peiran Ren, Xuansong Xie, and Lei Zhang. Pixel-aware stable diffusion for realistic image super-resolution and personalized stylization. *arXiv preprint arXiv:2308.14469*, 2023. 2, 3, 4, 5, 6, 8, 9, 10

[69] Jiahui Yu, Xin Li, Jing Yu Koh, Han Zhang, Ruoming Pang, James Qin, Alexander Ku, Yuanzhong Xu, Jason Baldridge, and Yonghui Wu. Vector-quantized image modeling with improved vqgan. *arXiv preprint arXiv:2110.04627*, 2021. 2

[70] Zongsheng Yue, Jianyi Wang, and Chen Change Loy. Resshift: Efficient diffusion model for image super-resolution by residual shifting. *arXiv preprint arXiv:2307.12348*, 2023. 3, 4, 5, 6, 8, 9, 10

[71] Kai Zhang, Wangmeng Zuo, Yunjin Chen, Deyu Meng, and Lei Zhang. Beyond a gaussian denoiser: Residual learning of deep cnn for image denoising. *IEEE transactions on image processing*, 26(7):3142–3155, 2017. 2

[72] Kai Zhang, Jingyun Liang, Luc Van Gool, and Radu Timofte. Designing a practical degradation model for deep blind image super-resolution. In *Proceedings of the IEEE/CVF International Conference on Computer Vision*, pages 4791–4800, 2021. 1, 2, 5, 6, 8, 9, 10

[73] Lvmin Zhang, Anyi Rao, and Maneesh Agrawala. Adding conditional control to text-to-image diffusion models. In *Proceedings of the IEEE/CVF International Conference on Computer Vision*, pages 3836–3847, 2023. 2, 3, 4, 5, 6

[74] Richard Zhang, Phillip Isola, Alexei A Efros, Eli Shechtman, and Oliver Wang. The unreasonable effectiveness of deep features as a perceptual metric. In *Proceedings of the IEEE conference on computer vision and pattern recognition*, pages 586–595, 2018. 6

[75] Xindong Zhang, Hui Zeng, Shi Guo, and Lei Zhang. Efficient long-range attention network for image super-resolution. *arXiv preprint arXiv:2203.06697*, 2022. 1, 2

[76] Yulun Zhang, Kunpeng Li, Kai Li, Lichen Wang, Bineng Zhong, and Yun Fu. Image super-resolution using very deep residual channel attention networks. In *Proceedings of the European conference on computer vision (ECCV)*, pages 286–301, 2018. 2

[77] Yulun Zhang, Yapeng Tian, Yu Kong, Bineng Zhong, and Yun Fu. Residual dense network for image super-resolution. In *Proceedings of the IEEE conference on computer vision and pattern recognition*, pages 2472–2481, 2018. 2

[78] Yuehan Zhang, Bo Ji, Jia Hao, and Angela Yao. Perception-distortion balanced ADMM optimization for single-image super-resolution. In *European Conference on Computer Vision*, pages 108–125. Springer, 2022. 1, 2

[79] Yi Zhang, Xiaoyu Shi, Dasong Li, Xiaogang Wang, Jian Wang, and Hongsheng Li. A unified conditional framework for diffusion-based image restoration. *arXiv preprint arXiv:2305.20049*, 2023. 3

[80] Huangjie Zheng, Pengcheng He, Weizhu Chen, and Mingyuan Zhou. Truncated diffusion probabilistic models and diffusion-based adversarial auto-encoders. *arXiv preprint arXiv:2202.09671*, 2022. 5

[81] Zixin Zhu, Xuelu Feng, Dongdong Chen, Jianmin Bao, Le Wang, Yinpeng Chen, Lu Yuan, and Gang Hua. Designing a better asymmetric vqgan for stablediffusion. *arXiv preprint arXiv:2306.04632*, 2023. 5